Article

Not peer-reviewed version

Graphitic Carbon Nitride Nanosheets Decorated Zinc-Cadmium Sulfide Type-II Heterojunction for Photocatalytic Hydrogen Production

Ammar Bin Yousaf [†], Muhammad Imran [†], Muhammad Farooq, Samaira Kausar, Samina Yasmeen, Peter Kasak [*]

Posted Date: 14 August 2023

doi: 10.20944/preprints202308.0977.v1

Keywords: Heterojunction; photocatalytic H2 production; carbon nitride; nanosheets; ZnCdS

Article

Graphitic Carbon Nitride Nanosheets Decorated Zinc-Cadmium Sulfide Type-II Heterojunctions for Photocatalytic Hydrogen Production

Ammar Bin Yousaf [1,†], Muhammad Imran [2,†], Muhammad Farooq [3,*], Samaira Kausar [4], Samina Yasmeen [4] and Peter Kasak [1,*]

[1] Center for Advanced Materials, Qatar University, Doha 2713, Qatar; ammar.schemist18@gmail.com, peter.kasak@qu.edu.qa
[2] Hefei National Laboratory for Physical Sciences at Microscale, University of Science and Technology of China, Hefei, Anhui 230026, PR China; imran345@mail.ustc.edu.cn
[3] Interdisciplinary Graduate School of Science and Technology, Shinshu University, Ueda 386-8567, Japan; 20hs109g@shinshu-u.ac.jp
[4] Department of Chemistry, National Science College, Satellite Town, Gujranwala 52250, Pakistan; samairakasr@gmail.com; samina.yasmn@gmail.com
* Correspondence: mufaroouk@gmail.com, 20hs109g@shinshu-u.ac.jp M.F.; peter.kasak@qu.edu.qaTel.: (974 4403 5674) P.K.
† These two authors contributed equally.

Abstract: In this study, we fabricated graphitic carbon nitride (*g*-C_3N_4) nanosheets with embedded ZnCdS nanoparticles to form a type II heterojunction using a facile synthesis approach, and used them for photocatalytic H_2 production. The morphologies, chemical structure, and optical properties of the obtained *g*-C_3N_4–ZnCdS samples were characterized by a battery of techniques, such as TEM, XRD, XPS, and UV-Vis DRS. The as-synthesized *g*-C_3N_4–ZnCdS photocatalyst exhibited the highest hydrogen production rate of 108.9 μmol·g^{-1}·h^{-1} compared to the individual components (*g*-C_3N_4: 13.5 μmol·g^{-1}·h^{-1}, ZnCdS: 45.3 μmol·g^{-1}·h^{-1}). The improvement of its photocatalytic activity can mainly be attributed to the heterojunction formation and resulting synergistic effect, which provided more channels for charge carrier migration and reduced the recombination of photogenerated electrons and holes. Meanwhile, the *g*-C_3N_4–ZnCdS heterojunction catalyst also showed higher stability over a number of repeated cycles. Our work provides insight into using *g*-C_3N_4 and metal sulfide in combination to develop low-cost, efficient, visiblelight-active hydrogen production photocatalysts.

Keywords: heterojunction; photocatalytic H_2 production; carbon nitride; nanosheets; ZnCdS

1. Introduction

The demand for energy is rising steadily as the world's population grows and living standards improve. Hydrogen is considered a clean, plentiful, and secure energy source to address this need [1]. The tremendous energy output of hydrogen combustion, which is far higher than that of gasoline or any other fossil fuel, makes it a better and more efficient alternate fuel. As no toxic byproducts are produced during hydrogen combustion it is also considered ecologically safe [2]. However, carbon dioxide is usually produced during the steam reforming of hydrocarbons and coal for hydrogen production. To avoid producing greenhouse gases, finding workable alternatives is essential. One viable solution to the present energy and environmental dilemma is using solar energy to produce hydrogen from water on the surface of a catalyst [3,4]. Semiconductor photocatalysts have been utilized widely for the photolysis of water, since their first use on the surface of TiO_2[5]. To maximize the use of solar power, various attempts have been made to find renewable, efficient photocatalysts with an excellent visible light response [6,7].

The carbon nitride (g-C_3N_4) graphitic material has been used as a C-related and a potential candidate with characteristics of metal-free photocatalyst in hydrogen evolution and organic degradation due to its suitable band gap (ca. 2.7 eV) [8]. Additionally, the electronic structure of the triazine units in g-C_3N_4 forms conjugated graphitic planes, which are very stable and responsive to visible light. However, its photocatalytic performance is severely impacted by both the negligible or no absorption under the visible portion of light irradiation (beyond 460 nm) & the fast recombination for the photo-induced charge carriers species [9]. To enhance the catalytic performance and promote the separation of photo-generated holes and electrons, another semiconductor is usually coupled with g-C_3N_4, such as g-C_3N_4/CdS, g-C_3N_4/TiO_2, g-C_3N_4/MoO_3, g-C_3N_4/$BiVO_4$, and g-C_3N_4/$InVO_4$[10–14]. However, the complex preparation process and catalyst deterioration over a few cycles make it harder to use on a broader industrial scale.

Among other alternatives, solid sulfide solutions such as $ZnIn_2S_4$, $CdIn_2S_4$, ZnCdS, and $Mn_xCd_{1-x}S$ have been used in photocatalytic hydrogen production because of their appropriate band gap, high visible light response, and tunable structure [15–18]. The easily tunable band structure and superior reducing ability of ZnCdS mean it stands out among the solid sulfide solutions [19]. However, it does have several drawbacks, including inadequate photo-generated carrier transmission efficiency, low solar energy consumption, and rapid electron-hole pair recombination, which severely restricts its photocatalytic efficacy [20,21]. The charge recombination efficiency and energy output can be improved by combining ZnCdS with another photocatalyst, offering more active sites and reaction sites to promote oxidation and reduction processes.

Herein, we demonstrated a simple strategy to fabricate g-C_3N_4 with ZnCdS to form a type II heterojunction. The conjugated graphitic planes of g-C_3N_4 nanosheets provided a large surface area for ZnCdS, which acted efficiently to use the charge carrier and enhance H_2 production.

2. Materials and Methods

2.1. Synthesis of g-C_3N_4 nanosheets

The preparation of g-C_3N_4 was performed in an alumina crucible with a cover, which could form a semi-closed atmosphere to prevent the sublimation of precursors. Melamine powder (3g) was placed into the crucible and heated to a temperature of 530 °C in a tube furnace with N_2 atmosphere. Then, the sample was naturally cooled to room temperature, collected, and stored for further use.

2.2. Synthesis of g-C_3N_4–ZnCdS heterojunction

The fabrication of g-C_3N_4 nanosheets with ZnCdS was achieved following our previous protocol, described briefly as [22]: first, g-C_3N_4 nanosheets were dispersed in DI water, and then the proper quantity of cadmium acetate and zinc acetate was slowly poured to the dispersion to achieve a 10wt% of ZnCdS on the g-C_3N_4 nanosheets. The mixture's pH was adjusted to 7.0. Subsequently, aqueous Na_2S solution was added dropwise. The samples were stirred at room temperature for 12 hours and extracted using centrifugation, washed with ethanol and water, and then dried overnight at 60 °C in a vacuum oven. The samples were heat treated at 400 °C under nitrogen flow and stored for further use.

2.3. Photo and electrochemical measurements

Measurement for photocatalytic hydrogen production was performed under visible light over as-synthesized samples by means of a vacuumed closed cell circulation system and catalyst powder, following the method described in our previous report [22]. The catalyst films for electrochemical measurements were prepared by applying an appropriate amount of catalyst suspension onto Ti foil. The current generated after photo-irradiation was detected amperometrically in cyclic performance by switching them on/off with a bias voltage of 0.5 V under visible light.

Preprints (www.preprints.org) | NOT PEER-REVIEWED | Posted: 14 August 2023 doi:10.20944/preprints202308.0977.v1

3. Results

The morphologies of the as-prepared samples were determined by transmission electron microscope (TEM). As can be seen in Figures 1 and S1, *g*-C_3N_4 exhibited planer nanosheet structure. ZnCdS were small irregular shaped nanoparticles distributed onto the nanosheets (yellow circles in Figure 1a). The high-resolution TEM image shows clear lattice dispersing of *g*-C_3N_4 and ZnCdS, with a value of 0.321 nm and 0.332 nm corresponding to a (002) plane distance (Figure 1b).

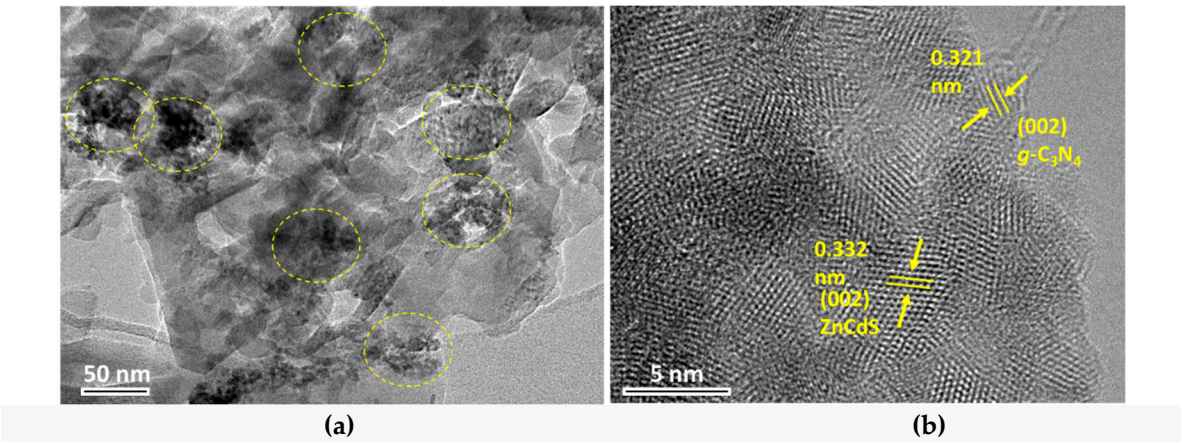

Figure 1. Transmission electron microscopy (TEM) images for as-prepared *g*-C_3N_4–ZnCdS samples (**a**) lower magnifications and (**b**) higher magnifications.

The XRD results of *g*-C_3N_4, ZnCdS, and *g*-C_3N_4–ZnCdS heterojunctionsare depicted in Figure 2. As shown in the case of pristine *g*-C_3N_4, the peak at 27.9° for the (002) diffraction plane was derived from interplanar stacking peaks of conjugated aromatic systems of C_3N_4. The peak was well matched with JCPDS # of 87-1526 of *g*-C_3N_4[23].The XRD results of ZnCdS showed peaks indexed at 27.34°, 45.32°, and 53.66° corresponding to the (111), (220), and (311) planes of the cubic phase of Zinc blend related to (ICSD # 80-0020). In the *g*-C_3N_4–ZnCdS heterojunction, there were no clear diffraction peaks of ZnCdS because of its relative low levels and smaller size compared to *g*-C_3N_4 [22].

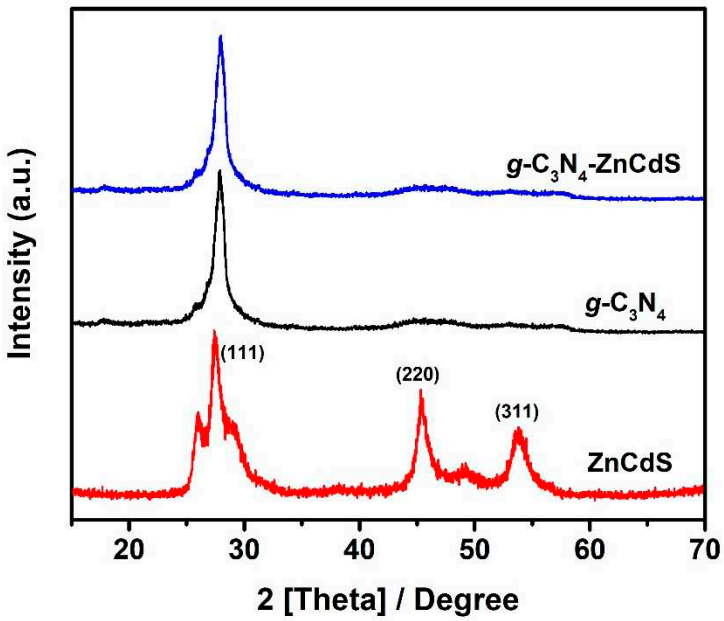

Figure 2. XRD spectrum of *g*-C_3N_4 (black line), ZnCdS (red line), and *g*-C_3N_4–ZnCdS (blue line) samples.

Preprints (www.preprints.org) | NOT PEER-REVIEWED | Posted: 14 August 2023 doi:10.20944/preprints202308.0977.v1

X-ray photoelectron spectroscopic (XPS) analysis was applied for determination of the elemental composition of the prepared catalyst and chemical state of particular elements. The survey spectrum of the *g*-C_3N_4–ZnCdS heterojunctions shown in Figure S2 indicates the sample primarily comprised C, N, Zn, Cd, and S elements. To further illustrate the elemental signal, high-resolution XPS spectra are provided in Figure 3. In the high-resolution XPS spectra of C1s shown in Figure 3a, the peak positioned at 284.8 eV can be related to sp^2 carbon atoms (C-C and N-C=N bonding) originating from the surface exotic C in the instrument. The 2nd peak located at 288.3 eV can be attributed to sp^3 hybridized C-bonded to nitrogen [C-$(N)_3$ of *g*-C_3N_4]. The high resolution XPS spectrum of N1s shows a large peak centered at 398.8 eV which can be ascribed to a nitrogen atom bonded to carbon [C-N=C], while the shoulder peak at 401.1 eV can readily be ascribed to N-$(C)_3$ and N-H [24,25] (Figure 3b).The high resolution XPS spectrum of Cd3d shows two spin-orbit components centered at 405.2 eV and 411.9 eV, which corresponded to $Cd3d_{5/2}$ and $Cd3d_{3/2}$, respectively (Figure 3b). Similarly, the Zn2p region also showed components indexed at 1022 eV and 1045 eV, ascribed to $Zn2p_{3/2}$and $Zn2p_{1/2}$, respectively (Figure 3c). Figure 3d denoted the high-resolution spectra of S2p that exhibit a peak centered at 161.87 eV, that is attributed to the S^{2-} valent state of S in the ZnCdS segment. All the peaks are well-matched with the values reported previously for ZnCdS [26].

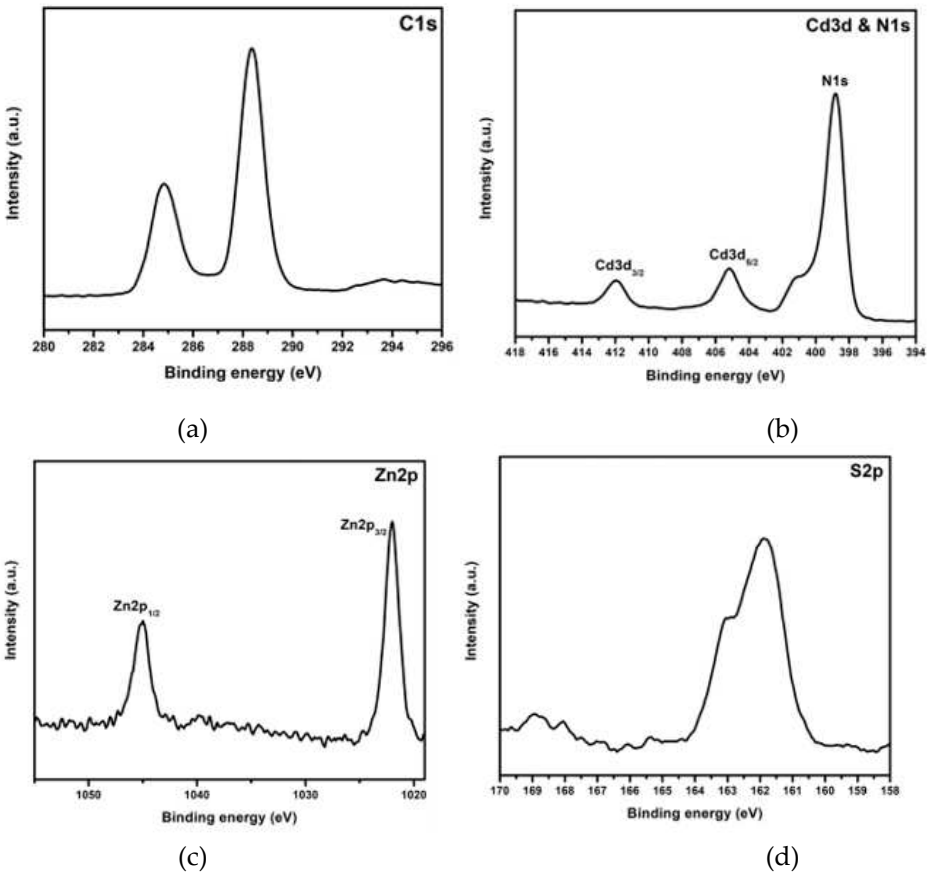

Figure 3. High resolution XPS spectrum for a *g*-C_3N_4–ZnCdS sample.Scans for (**a**) C1s, (**b**)Cd3d and N1s, (**c**)Zn2p, and (**d**) S2p regions.

The optical properties of pure *g*-C_3N_4 nanosheets, ZnCdS nanoparticles, and *g*-C_3N_4–ZnCdS heterojunctions were measured with UV-vis DRS. As shown in Figure 4a, the characteristic absorption peak of pure *g*-C_3N_4 nanosheets was at about 400 nm, arising from the intrinsic band gap of *g*-C_3N_4 at about 2.7 eV, that has low visible light absorption characteristic itself. On the other hand, ZnCdS showed strong absorption towards the visible region and the absorption edge extended towards 500 nm. After introducing ZnCdS nanoparticles into g-C_3N_4 nanosheets, heterojunction formation showed increased absorption intensity compared to bare *g*-C_3N_4 nanosheets, and the absorption edge also moved towards the visible region. Figure 4B displays the related *Tauc* plots and

Preprints (www.preprints.org) | NOT PEER-REVIEWED | Posted: 14 August 2023 doi:10.20944/preprints202308.0977.v1

all samples was examined for evaluation of the band gap energies. Band gap energy were obtained from analysis of the plot and the intercept of the tangent of the curve $(\alpha h\nu)^2$ vs. $(h\nu)$ on the X-axis, as previously reported [27]. The calculated band gap energies for samples of *g*-C_3N_4 nanosheets, ZnCdS nanoparticles, and *g*-C_3N_4–ZnCdS heterojunctions were determined from *Tauc* plot to be 2.72 eV, 2.25 eV, and 2.60 eV, respectively (Figure 4b). After the introduction of ZnCdS nanoparticles, the large band gap of *g*-C_3N_4 nanosheets decreased, which supported its photocatalytic performance.

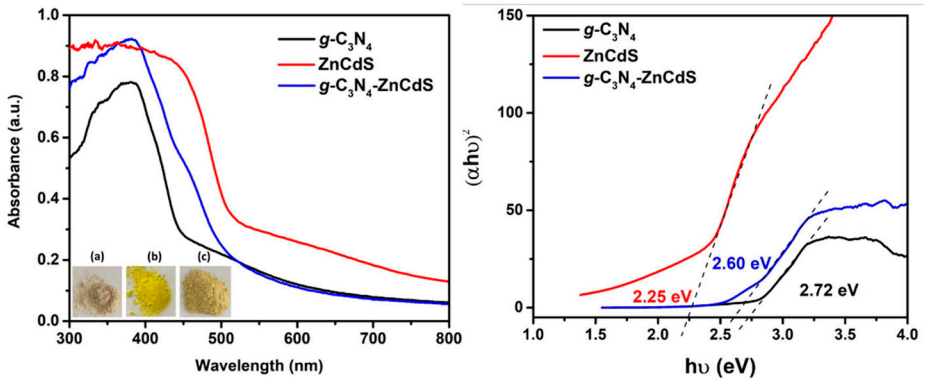

(a) (b)

Figure 4. (**a**) UV–visible diffuse reflectance spectra (DRS) and (**b**) related *tauc* plot for *g*-C_3N_4, ZnCdS, and *g*-C_3N_4–ZnCdS. The insets (a) are the images of the samples of *g*-C_3N_4 (a), ZnCdS (b), and *g*-C_3N_4–ZnCdS (c).

The photocatalytic hydrogen evolution ability of bare *g*-C_3N_4 nanosheets, ZnCdS nanoparticles, and *g*-C_3N_4–ZnCdS heterojunctions was evaluated under visible light irradiation, as shown in Figure 5a. The H_2 production rate for*g*-C_3N_4 was observed at 13.5 $\mu mol \cdot g^{-1} \cdot h^{-1}$. In comparison, ZnCdS was 45.3 $\mu mol \cdot g^{-1} \cdot h^{-1}$. Compared to bare samples, the *g*-C_3N_4–ZnCdS heterojunction showed an increase in photocatalytic H_2 production (108.9 $\mu mol \cdot g^{-1} \cdot h^{-1}$). This was about eight times higher than *g*-C_3N_4 and 2.4 times higher than ZnCdS. The increase in the H_2 production rate indicated that a heterojunction formed between the individual components, which facilitated the mobility of the charge carrier and enhanced the photocatalytic performance. Another issue to be considered in the applicability of photocatalysts is their performance in reusability. Therefore, reusability experiments were performed for *g*-C_3N_4–ZnCdS heterojunctions, and after each run, the catalyst was recovered by centrifugation, washed with water and ethanol, and reused. As displayed in Figure 5b, the hydrogen generation rate was remarkably stable over five cycles (94% retention rate with a value decrease from 108.9 to 102.3 $\mu mol \cdot g^{-1} \cdot h^{-1}$), indicating the excellent stability and sustainable utilization of the photocatalyst.

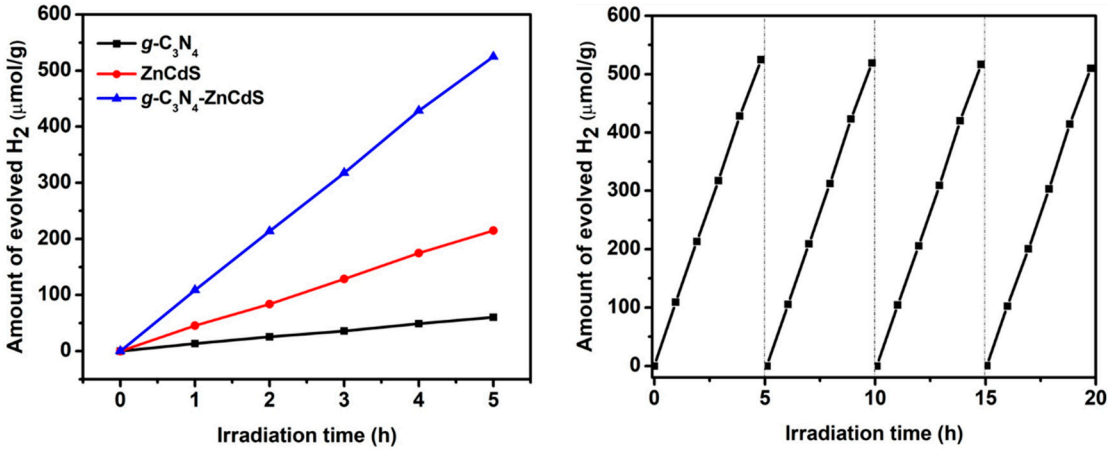

Preprints (www.preprints.org) | NOT PEER-REVIEWED | Posted: 14 August 2023 doi:10.20944/preprints202308.0977.v1

Figure 5. (**a**) Photocatalytic H_2 evolution activities from water splitting on samples from *g*-C_3N_4 nanosheets, ZnCdS nanoparticles, and *g*-C_3N_4–ZnCdS under visible light illumination ($\lambda \geq 420$ nm) over 5 hours. (b) Cyclic tests for photocatalytic H_2 evolution activities from water solution on *g*-C_3N_4–ZnCdS for four consecutive cycles.

In order to explore how the*g*-C_3N_4–ZnCdS heterojunction shows better photocatalytic performance compared to individual components, the electron transfer mechanism was revealed, as shown in Figure 6. The conduction and valence band potentials of a photocatalyst can be calculated by the following equations:

$$E_{VB} = X - E_e + 0.5E_g \quad (1)$$

$$E_{CB} = E_{VB} - E_g \quad (2)$$

Where E_{VB} and E_{CB} represent the valence and conduction band potentials, respectively. E_g is the band-gap energy, E_e denotes the energy of the free electrons on the hydrogen scale, and X represents the absolute electronegativity [28]. By using equations 1 and 2, the conduction and valence band potentials for ZnCdS were determinated as E_{VB} = 1.85 eV and E_{CB} = -0.39 eV, respectively, while for *g*-C_3N_4, they were calculated as E_{VB} = 1.59 eV and E_{CB} = -1.13 eV. Both the valence and conduction bands for ZnCdS were lower compared to *g*-C_3N_4, which facilitates the formation of type II heterojunctions. Upon visible light irradiation, both ZnCdS and *g*-C_3N_4 can be excited, and then electrons from the CB of *g*-C_3N_4 can be transferred into the CB of ZnCdS, which then react with H^+ for H_2 production. At the same time, the photo-induced holes of *g*-C_3N_4 and ZnCdS can be used by oxidizing agents [29,30].

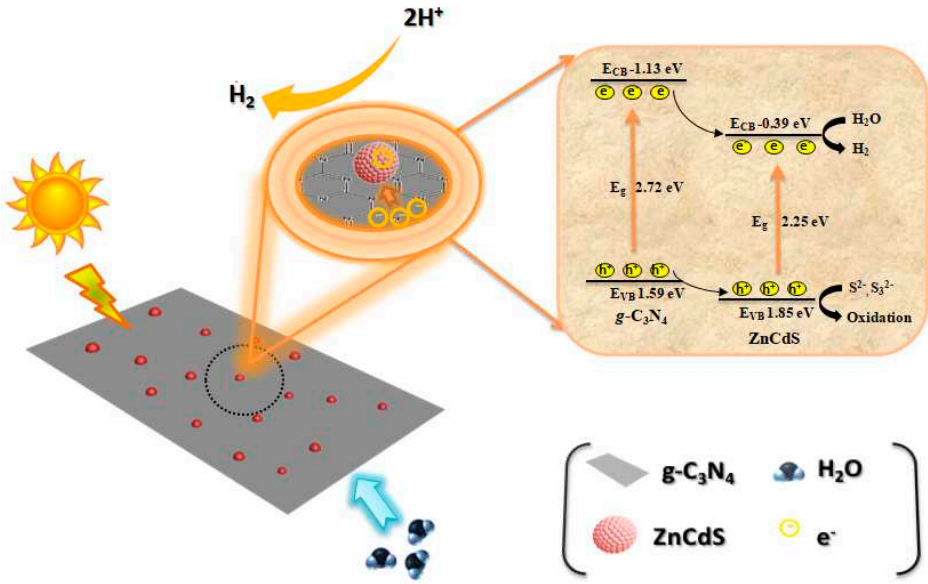

Figure 6. A schematic representation showing the photocatalytic process, band positions, and charge transfer process for g-C_3N_4–ZnCdS.

The photocatalytic conjecture was further verified by transient photocurrent response. It was recorded for *g*-C_3N_4, ZnCdS, and *g*-C_3N_4–ZnCdS heterojunctions. Figure 7A shows *I-t* curves for as-synthesized electrodes film with five ON-OFF intermittent visiblelight irradiation consecutive cycles [31]. The responses of photocurrent were appeared in all the electrodes instantly as the light was turned on, then rapidly declined to zero (nearly) as the light was off, which was reproducible and stable. With the similar conditions of irradiation, the photo-current value of the ZnCdS electrode was about twice to that of bare *g*-C_3N_4, suggesting there was low-recombination and fast migration of photogenerated electron on the*g*-C_3N_4 nanosheets. Additionally, after heterojunction formation between individual components, *g*-C_3N_4–ZnCdS showed a much higher photocurrent value by about 2.6 times, confirming the photogenerated electrons from the *g*-C_3N_4 were attacking part in the electron transfer process and shifted to the CB of ZnCdS efficiently.

Preprints (www.preprints.org) | NOT PEER-REVIEWED | Posted: 14 August 2023 doi:10.20944/preprints202308.0977.v1

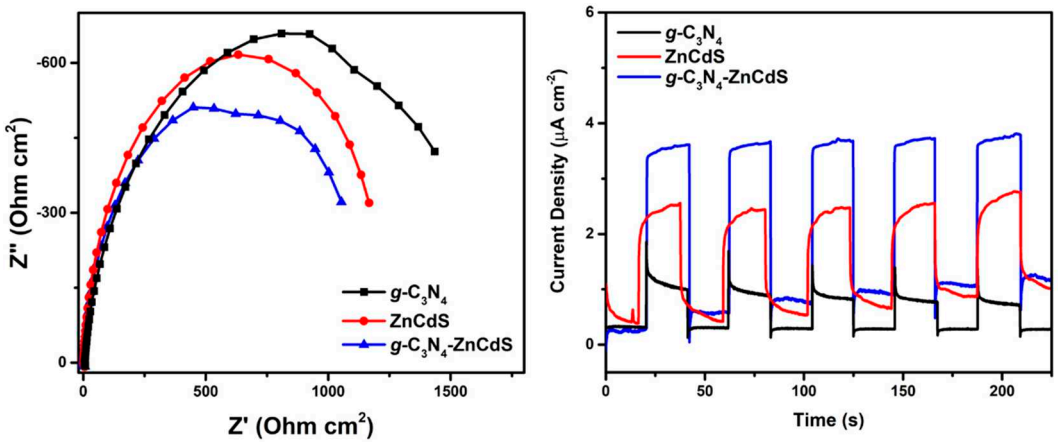

(a) (b)

Figure 7. (**a**) Nyquist plots from EIS measurement of *g*-C_3N_4, ZnCdS, and g-C_3N_4–ZnCdS. (**b**) Cyclic performance of the response of the current from as-synthetized photocatalysts vs. time for *g*-C_3N_4, ZnCdS, and *g*-C_3N_4–ZnCdS (irradiated at $\lambda \geq 420$ nm).

EIS is another efficient technique to observe the charge transfer efficiency and the interface reaction ability, which explains charge transfer resistance [32]. Figure 7B shows the Nyquist plots of *g*-C_3N_4, ZnCdS, and *g*-C_3N_4–ZnCdS heterojunctions. The smaller diameter implied a low impedance and fast interface charge transfer. The *g*-C_3N_4–ZnCdS heterojunction had the smallest diameter compared to bare samples, which also showed less charge transfer resistance and coincided well with photocurrent response results. Overall, our results showed that the heterojunction formation between *g*-C_3N_4 and ZnCdS enables less recombination and faster photogenerated electron migration, resulting in a higher photocatalytic performance and enhanced durability.

5. Conclusions

In summary, we successfully synthesized *g*-C_3N_4–ZnCdS heterojunctions via a facile physical mixture and calcination method. The as-synthesized material was characterized using battery of the techniques, such as TEM, XRD, XPS, and UV−vis DRS. The catalysts were used for photocatalytic H_2 production, and among all synthesized materials, *g*-C_3N_4–ZnCdS revealed the enhanced UV vis induced photocatalytic performance, with a hydrogen production of 108.9 $\mu mol \cdot g^{-1} \cdot h^{-1}$ under the visible light, which was significantly higher compared to individual components. The photocatalysts also possessed excellent repeatability over five cycles, with a mere 6% decrease in photocatalytic activity. The higher and modified photocatalytic performance mainly depended on synergistic effects among the components and heterojunction formation. The transient photocurrent responses and EIS further supported the enhanced performance due to decreased electron-hole recombination and low charge transfer resistance. The facile synthetic approach and better performance of *g*-C_3N_4–ZnCdSprovides new opportunities for further study of the photocatalytic process of coupled semiconductors for hydrogen production.

Supplementary Materials: The following supporting information can be downloaded at the website of this paper posted on Preprints.org. S1 Material and methods; Figure S1: Low-resolution TEM image of the*g*-C_3N_4–ZnCdS catalyst; Figure S2: XPS full scan survey for the*g*-C_3N_4–ZnCdS catalyst.

Author Contributions: Conceptualization and methodology, A. B.Y. and M. I.; formal analysis, investigation, resources and data curation, all authors; writing—original draft preparation, A.B.Y. and M. I.; writing—review and editing, P.K..; visualization, all authors; supervision, M.F. and P.K.; project administration P.K. and M.F..; funding acquisition, P.K. All authors have read and agreed to the published version of the manuscript.

Funding: The authors acknowledge the financial support made possible by Qatar University grant # QUCG-CAM-22/23-504. The finding achieved herein are solely the responsibility of the authors.

Institutional Review Board Statement: Not applicable.

Informed Consent Statement: Not applicable.

Data Availability Statement: The data presented in this study are available on request from the corresponding authors.

Acknowledgments: The authors would like to thank the Center for Advanced Materials, Qatar University, for facilities support.

Conflicts of Interest: The authors declare no conflict of interest.

References

1. Christoforidis, K.C.; Fornasiero P. Photocatalytic Hydrogen Production: A Rift into the Future Energy Supply. *ChemCatChem***2017**, *9*, 1523–1544.
2. Corredor, J.; Rivero, M.J.; Rangel, C.M.; Gloaguen, F.; Ortiz, I. Comprehensive review and future perspectives on the photocatalytic hydrogen production.*J Chem Technol Biotechnol***2019**, *94*,3049–3063.
3. Teets, T.S.; Nocera, D.G. Photocatalytic hydrogen production. *Chem. Commun.* **2011**, *47*, 9268–9274.
4. Yukesh Kannah, R.; Kavitha, S.; Preethi; Parthiba Karthikeyan, O.; Kumar, G.; Dai-Viet, N.V.; Rajesh banu, J. Techno-economic assessment of various hydrogen production methods – A review. *Bioresour. Technol.* **2021**, *319*, 124175.
5. Fujishima, A.; Honda K. Electrochemical Photolysis of Water at a Semiconductor Electrode. *Nature* **1972**, *238*, 37–38.
6. Hisatomi, T.; Kubota, J.; Domen, K. Recent advances in semiconductors for photocatalytic and photoelectrochemical water splitting. *Chem. Soc. Rev.***2014**, *43*, 7520–7535.
7. Chen, X.; Shen, S.; Guo, L.; Mao, S.S. Semiconductor-based photocatalytic hydrogen generation. *Chem. Rev.***2010**, *110*, 6503–6570.
8. Ong, W.J.; Tan. L.L.; Ng. Y.H.; Yong, S.T.; Chai, S.P. Graphitic Carbon Nitride (g-C3N4)-Based Photocatalysts for Artificial Photosynthesis and Environmental Remediation: Are We a Step Closer to Achieving Sustainability? *Chem. Rev.* **2016**, *116*, 7159–7329.
9. Thomas, A.; Fischer, A.; Goettmann, F.; Antonietti, M.; Müller, J.O.; Schlögl, R.;Carlsson, J. M. Graphitic carbon nitride materials: Variation of structure and morphology and their use as metal-free catalysts. *J. Mater. Chem.* **2008**,*18*, 4893–4908.
10. Acharya, R.; Parida, K. A review on TiO2/g-C3N4 visible-light-responsive photocatalysts for sustainable energy generation and environmental remediation. *J. Environ. Chem. Eng.***2020**, *8*, 103896.
11. Vu, N.N.; Kaliaguine S.; Do, T.O. Synthesis of the g-C3N4/CdS Nanocomposite with a Chemically Bonded Interface for Enhanced Sunlig,ht-Driven CO2Photoreduction. *ACS Appl. Energy Mater.* **2020**, *3*, 6422–6433.
12. Huang, L.; Xu, H.; Zhang, R.; Cheng, X.; Xia, J.; Xu, Y.;Li, H. Synthesis and characterization of g-C3N4/MoO3 photocatalyst with improved visible-light photoactivity. *Appl. Surf. Sci.***2013**, *283*, 25–32.
13. Li, Y.Y.; Qin, T.; Chen, W.; Huang, M.; Xu, J.; Lv, J. Construction of a Switchable g-C3N4/BiVO4Heterojunction from the Z-Scheme to the Type II by Incorporation of Pyromellitic Diimide. *Cryst. Growth Des.***2022**, *22*, 1645–1653.
14. Hu, B.; Cai, F.; Chen, T.; Fan, M.; Song, C.; Yan, X.;Shi, W. Hydrothermal Synthesis g-C3N4/Nano-InVO4 Nanocomposites and Enhanced Photocatalytic Activity for Hydrogen Production under Visible Light Irradiation. *ACS Appl. Mater. Interfaces***2015**, *7*, 18247–18256.
15. Peng, H.; Du, Y.; Zheng, X.; Wen, J. High-temperature sulfurized synthesis of MnxCd1-xS composites for enhancing solar-light driven H2 evolution. *Int. J. Hydrogen Energy* **2022**, *47*, 9925–9933.
16. Chen, J.; Chen, J.; Li, Y. Hollow ZnCdS dodecahedral cages for highly efficient visible-light-driven hydrogen generation. *J. Mater. Chem. A***2017**, *5*, 24116–24125.
17. He, J.; Li, B.; Yu, J.; Qiao, L.; Li, S.; Zu, X.; Xiang, X. Ultra-thin CdIn2S4 nanosheets with nanoholes for efficient photocatalytic hydrogen evolution. *Opt. Mater. (Amst)* **2020**,*108*, 2–6.
18. Shi, X.; Dai, C.; Wang, X.; Hu, J.; Zhang, J.; Zheng L.; et al. Protruding Pt single-sites on hexagonal ZnIn2S4 to accelerate photocatalytic hydrogen evolution. *Nat. Commun.***2022**, *13*, 1–10.
19. Li, Q.; Meng, H.; Zhou, P.; Zheng, Y.; Wang, J.; Yu, J.; et al. $Zn_{1-x}Cd_xS$ solid solutions with controlled bandgap and enhanced visible-light photocatalytic H2-production activity. *ACS Catal.* **2013**,*3*, 882–889.
20. Chen, R.; Li, K.; Zhu, X.S.; Xie, S.L.; Dong, L.Z.; Li, S.L.; et al. In situ synthesis of porous ZnO-embedded Zn1-xCdxS/CdS heterostructures for enhanced photocatalytic activity. *CrystEngComm* **2016**, *18*, 1446–52.

21. Li, K.; Chen, R.; Li, S.L.; Xie, S.L.; Dong, L.Z.; Kang, Z.H.; et al. Engineering Zn1-xCdxS/CdS Heterostructures with Enhanced Photocatalytic Activity. *ACS Appl. Mater. Interfaces* **2016**, *8*, 14535–114541.
22. Imran, M.; Yousaf, A Bin.; Kasak, P.; Zeb, A.; Zaidi, S.J. Highly efficient sustainable photocatalytic Z-scheme hydrogen production from an A-Fe2O3 engineered ZnCdS heterostructure. *J. Catal.* **2017**, *353*, 81–88.
23. Vijayan, M.; Manikandan, V.; Rajkumar, C.; Hatamleh, A.A.; Alnafisi, B.K.; Easwaran, G.; et al. Constructing Z-scheme g-C3N4/TiO2 heterostructure for promoting degradation of the hazardous dye pollutants. *Chemosphere* **2023**, *311*,c136928.
24. Ding, J.; Sun, X.; Wang, Q.; Li, D.S.; Li X.; Li, X.; et al. Plasma synthesis of Pt/g-C3N4 photocatalysts with enhanced photocatalytic hydrogen generation. *J. Alloys Compd.* **2021**, *873*, 159871.
25. Tan, L.; Xu, J.; Zhang, X.; Hang, Z.; Jia, Y.; Wang, S. Synthesis of g-C3N4/CeO 2 nanocomposites with improved catalytic activity on the thermal decomposition of ammonium perchlorate. *Appl. Surf. Sci.***2015**, *356*, 447–453.
26. Hao, X.; Xiang, D.; Jin, Z. Zn-Vacancy Engineered S-Scheme ZnCdS/ZnS Photocatalyst for Highly Efficient Photocatalytic H2 Evolution. ChemCatChem **2021**, *13*, 4738–4750.
27. Yang, Q, Yu, L.; Zhao, X.; Wang, Y.; Zhu, H.; Zhang, Y. Highly stable γ-NiOOH/ZnCdS photocatalyst for efficient hydrogen evolution. *Int. J. Hydrogen Energy***2022**, *47*, 27516–27526.
28. Butler, M.A.; Ginley, D.S. Prediction of Flatband Potentials at Semiconductor-Electrolyte Interfaces from Atomic Electronegativities. *J. Electrochem. Soc.* **1978**, *125*, 228–232.
29. Ge, F.; Li, X.; Wu, M.; Ding, H.; Li, X. A type II heterojunction α-Fe2O3/g-C3N4 for the heterogeneous photo-Fenton degradation of phenol. *RSC Adv.***2022**, *12*, 8300–8309.
30. Wang, Y.; Fiaz, M.; Kim, J.; Carl, N.; Kim, Y.K. Kinetic Evidence for Type-II Heterojunction and Z-Scheme Interactions in g-C3N4/TiO2Nanotube-Based Photocatalysts in Photocatalytic Hydrogen Evolution. *ACS Appl. Energy Mater.* **2023**, *6*, 5197–206.
31. Serafin, J.; Ouzzine, M.; Sreńscek-Nazzal, J.; Llorca, J. Photocatalytic hydrogen production from alcohol aqueous solutions over TiO2-activated carbon composites decorated with Au and Pt. *J.Photochem. Photobiol. A Chem.* **2022**, *425*, 113726.
32. Dong, Z.; Wu, Y.; Thirugnanam, N.; Li, G. Double Z-scheme ZnO/ZnS/g-C3N4 ternary structure for efficient photocatalytic H 2 production. *Appl. Surf. Sci.* **2018**, *430*, 293–300.